1   **Ridge Subduction and Afterslip Control Aftershock Distribution of the 2016 Mw 7.8**
2   **Ecuador Earthquake**
3
4   H. Agurto-Detzel, Y. Font, P. Charvis, M. Régnier, A. Rietbrock, D. Ambrois, M. Paulatto,
5   A. Alvarado, S. Beck, M.J. Hernandez, S. Hernandez, M. Hoskins, S. León-Ríos, C. Lynner,
6   A. Meltzer, D. Mercerat, F. Michaud, J.M. Nocquet, F. Rolandone, M. Ruiz, L. Soto-Cordero
7
8   Corresponding author: HAD   agurto@geoazur.unice.fr   h.agurto.detzel@gmail.com
9
10
11 **Abstract**

12 We characterise the aftershock sequence following the 2016 Mw=7.8 Pedernales earthquake.

13 More than 10,000 events were detected and located, with magnitudes up to 6.9. Most of the

14 aftershock seismicity results from interplate thrust faulting, but we also observe a few normal

15 and strike-slip mechanisms. Seismicity extends for more than 300 km along strike, and is

16 constrained between the trench and the maximum depth of the coseismic rupture. The most

17 striking feature is the presence of three seismicity bands, perpendicular to the trench, which

18 are also observed during the interseismic period. Additionally, we observe a linear

19 dependency between the temporal evolution of afterslip and aftershocks. We also find a

20 temporal semi-logarithmic expansion of aftershock seismicity along strike and dip directions,

21 further indicating that their occurrence is modulated by afterslip. Lastly, we observe that the

22 spatial distribution of seismic and aseismic slip processes is correlated to the distribution of

23 bathymetric anomalies associated with the northern flank of the Carnegie Ridge, suggesting

24 that slip in the area could be influenced by the relief of the subducting seafloor. To explain

25 our observations, we propose a conceptual model in which the Ecuadorian margin is subject

26 to a bimodal slip mode, with distributed seismic and aseismic slip mechanically controlled by

27 the subduction of a rough oceanic relief. Our study sheds new light on the mechanics of

28 subduction, relevant for convergent margins with a complex and heterogeneous structure

29 such as the Ecuadorian margin.

30 **Keywords:** Aftershock; Subduction; Afterslip; Ecuador; Carnegie Ridge; Seafloor Relief;

1. Introduction

The largest earthquakes on Earth occur in subduction zones, which also host a diversity of processes including seismic and aseismic slip along the subduction interface (e.g. Bilek and Lay, 2018, and references therein). What controls the occurrence and distribution of these phenomena remains an outstanding problem in Earth sciences. One way to gain a better insight into the nature of the subduction mechanism and the physical medium that host them, is by studying the aftershocks sequence that follows a large megathrust earthquake. Moreover, the high rate of seismicity during aftershock sequences, combined with recent technological and logistical improvements in seismological network deployments and data processing (e.g. Beck et al., 2014), allows us to collect and analyse vast amounts of data with increased spatio-temporal resolution.

Aftershocks occur either because of the release of residual stresses on the mainshock fault and surrounding medium, or as a result of static or dynamic stress perturbations due to the co-seismic rupture and subsequent aftershocks (e.g. Das and Henry, 2003; Freed, 2005). Consequently, aftershocks can provide an independent constraint in the shape and extension of the rupture area and interface heterogeneities, as well as help us identify areas of partially released and/or accumulated stress over the megathrust interface following the mainshock, thus delineating potential source areas for future earthquakes.

The often intricate distribution of aftershocks accounts for a complex distribution of remaining stresses and interface heterogeneities following the mainshock. For instance, after the 2005 Mw=8.7 Nias-Simeulue earthquake in Sumatra, Hsu et al. (2006) found that aftershocks clustered in the boundary area between the coseismic rupture and the afterslip area, with afterslip concentrated mostly up-dip of the coseismic rupture. Furthermore, it is often observed that regions of large co-seismic slip tend to have little seismicity after the

56 mainshock rupture, whilst the largest aftershocks concentrate around the patches of large co-

57 seismic slip (e.g. Das and Henry, 2003; Rietbrock et al., 2012; Agurto et al., 2012; Wetzler et

58 al., 2018). On the other hand, aftershock activity is not only limited to the megathrust

59 interface, but also to the surrounding seismogenic volume, often showing a diversity of focal

60 mechanisms and complex interactions between activity in the slab and in the overriding plate

61 (e.g. Asano et al., 2011). Lastly, for some subduction earthquakes, such as the 2011 Tohoku,

62 Japan earthquake, the reduction of shear stresses after the mainshock is such that it produces

63 a rotation of the deviatoric stress field, potentially causing extensional earthquakes in a

64 previously compressional setting (e.g. Ryder et al., 2012; Hardebeck, 2012).

65

66 Moreover, the physics behind aftershock generation is still not fully understood. Aftershocks

67 were first described and used as a proxy for the mainshock rupture extension, and

68 subsequently explained as ruptures on surrounding faults due to the re-distribution of strain

69 energy following the mainshock. Consequently, aftershocks triggering mechanism would be

70 related to dynamic and/or static stress transfers, following the mainshock and subsequent

71 aftershocks (Stein, 1999). More recently, observational and theoretical studies have proposed

72 that afterslip plays an important role in the occurrence and distribution of aftershocks (e.g.

73 Henry and Das, 2001; Perfettini et al., 2018). For example, following the 2005 Mw=8.7 Nias-

74 Simeulue earthquake in Sumatra, Hsu et al. (2006) found that the cumulative number of

75 aftershocks increased linearly with the postseismic displacement, suggesting that the

76 temporal evolution of aftershocks is governed by afterslip.

77

78 On the 16 of April 2016, a Mw=7.8 earthquake struck the coast of northern Ecuador

79 rupturing a ~100 km-long asperity of the interface between the Nazca plate and South

80 America (Nocquet et al., 2017). Shortly after the mainshock, we deployed an amphibious

81   temporary network of seismic stations to monitor the evolution of the seismic activity. In this

82   paper, we benefit from the continuous seismic waveform dataset acquired during one year of

83   the aftershock deployment to explore the distribution of hypocentral locations and

84   magnitudes for the Pedernales sequence. We also use full waveform inversions to compute

85   moment tensors for a selection of events, providing a seismotectonic constraint to the

86   characterization of the sequence. We discuss our results in the light of the earthquake cycle,

87   exploring the relations between seismic and aseismic processes within the context of a

88   subduction zone with highly heterogeneous frictional properties. Finally, we present a

89   conceptual model in which we explain the distribution and diversity of slip processes in the

90   Ecuadorian margin, and the control factors that affect them.

91

92   *1.1 Seismotectonic context and previous studies*

93   The Ecuador-Colombia subduction margin has generated four large tsunamigenic megathrust

94   earthquakes (Mw > 7.5) in the 20th century. In 1906, an Mw ~8.8 event (the largest thus far

95   documented offshore Ecuador) ruptured a roughly 500 km-long segment of the margin,

96   causing widespread damage and tsunami waves (Kanamori and McNally, 1982). Subsequent

97   events occurred in 1942 (Mw 7.8), 1958 (Mw 7.7) and 1979 (Mw 8.2; Kanamori and

98   McNally, 1982; Beck and Ruff, 1984), partially overlapping the rupture area of the 1906

99   event. This sequence of three earthquakes presented a northward migration pattern (Fig. 1),

100   and the sum of their combined seismic moments accounts for only a fifth of the moment

101   released by the 1906 event (Keller, 1972; Kanamori and McNally, 1982). This would imply

102   that the 1906 event not only ruptured the other three isolated asperities simultaneously, but

103   also broke the adjacent subduction interface which otherwise creeps during the interseismic

104   period.

105

106   The area that ruptured in 2016 had already been identified as a highly coupled region (Chlieh

107   et al., 2014; Nocquet et al., 2014), and the same asperity had allegedly been ruptured by the

108   earthquake of 1942 (Nocquet et al., 2017). In this region, the convergence rate between

109   Nazca and South America is 58 mm/yr, which is partially accommodated by the north-eastern

110   motion of the North-Andean sliver, resulting in a slip rate of 46 mm yr^{-1} at the megathrust

111   (Chlieh et al., 2014; Nocquet et al., 2014). Also, this area is located within the northern flank

112   of the aseismic Carnegie Ridge (hereafter CR), which currently subducts beneath South

113   America between 0° to 2.5° lat. S.

114

115   To date, several co-seismic slip models of the 2016 earthquake have been published based on

116   a complete or partial use of teleseismic, tsunami, GPS, InSAR and regional accelerometric

117   data (e.g. Ye et al., 2016; Nocquet et al., 2017; Yoshimoto et al., 2017; Gombert et al., 2018

118   and references within). All models have in common an extension of the rupture area of

119   roughly 100 km along strike, a southward propagation rupture, and the presence of two

120   patches of high coseismic slip with no shallow slip near the trench. They differ, however, in

121   the maximum and average amount of slip, with maximum slip ranging from 2 m (Yoshimoto

122   et al., 2017) to 6-7 m (Nocquet et al., 2017; Gombert et al., 2018). These last two models are

123   very similar regarding magnitude and distribution of the co-seismic slip, and are the most

124   comprehensive up to date in terms of diversity of used datasets and methodology.

125

126   Previous studies using geodetic and seismological data highlight the diverse nature of slip

127   processes in the interseismic period. Font et al. (2013) produced a seismicity catalogue for a

128   13-yr period based on locations in a 3-D a priori velocity model. Vallée et al. (2013)

129   characterized a one-week-long slow slip event (SSE), accompanied by a seismic swarm, that

130   occurred in August 2010 below La Plata Island (hereafter LPI), south of the 2016 rupture.

131 Similarly, Vaca et al. (2018) described a six-week-long SSE accompanied by a seismic

132 swarm that occurred between December 2013 and January 2014 at the northern limit of the

133 2016 rupture, arguing that this area acted as a barrier for the 2016 rupture propagation

134 northwards. Finally, Segovia et al. (2018) studied the seismicity distribution during a two-

135 year experiment in the south of the region, describing the interface geometry, and associating

136 swarm-like activity to a SSE below LPI.

137

138 **2. Data and Methods**

139 *Earthquake rapid response deployment*

140 Following the Pedernales earthquake, an international effort involving institutions from

141 Ecuador (IG-EPN), France (Géoazur, Cerema, IRD and CNRS), the UK (U. of Liverpool)

142 and the USA (IRIS, U. of Lehigh, U. of Arizona) rapidly installed a network of 50 inland

143 stations and 10 ocean-bottom seismometers (OBS) to record for one year after the mainshock

144 (Fig. 2; Meltzer et al., 2018). This temporary deployment complemented the permanent

145 Ecuadorian network (Alvarado et al., 2018). Instruments included broadband, intermediate

146 and short period stations, in addition to some accelerometers from the Ecuadorian network,

147 all recording at a sampling rate of 100 Hz or higher.

148

149 *Data processing*

150 The continuous waveforms were collected and archived in mini-seed format. They were

151 processed using the software package *SEISCOMP3* (SC3; https://www.seiscomp3.org) which

152 provides in-built capacity to detect, associate and locate seismic events including the

153 calculation of magnitudes. Although SC3 is primarily designed for real-time monitoring with

154 continuous injection of data, it can also be used in 'playback mode', that is, injecting and

155 processing the whole of the collected data at once. Parameterization of the different SC3

156   modules is critical, and therefore we adopted an empirical approach in which several tests

157   were systematically performed looking for the best set of parameters that would maximize

158   the number of real events while minimizing the number of false detections. Control days, for

159   which we manually detected events, were used to asses this fine-tuning process. Additionally,

160   we visually inspected the detected events and discarded false detections as well as classified

161   real events into first and second quality events according to the number and accuracy of their

162   automatic picks (see Sup. Mat.).

163

164   The workflow was as follows: after injection of the continuous waveform dataset, detection

165   of arrival times was performed using a standard STA/LTA algorithm for P-phases and the

166   AIC picker implemented in SC3 for S-phases, on band-pass filtered waveforms (1-10 Hz for

167   seismometers; 1-8 Hz for accelerometers and OBS). Subsequently, we used the SC3 module

168   *SCANLOC,* which is based on the cluster-search algorithm *DBSCAN* (Easter et al., 1996), to

169   associate picks and locate events. Relocation of these initial events was performed using the

170   *NonLinLoc* (NLL) algorithm (Lomax, 2000) configured in standard global mode. The visual

171   quality-inspection described above was carried out on these preliminary locations. Finally,

172   the whole set of events was relocated outside SC3 using NLL configured in regional mode

173   (Cartesian coordinates) and a simplified velocity model taken from a newly derived 1-D

174   velocity structure for the region (León-Ríos et al., 2017; see Sup. Mat.).

175

176   Initially, a total of 15,233 aftershocks were detected and located for the period between April

177   16 2016 to April 30 2017. Visual analysis of seismic sections was performed to identify and

178   discard false detections, spurious events, and to assess the pick quality to assemble a high-

179   quality subset of events. After this visual inspection, a total of 4,963 (33%) events were

180   discarded as false detections or spurious events (poor signal and/or too noisy). The 10,270

181   events left were classified into two categories according to their picks and location quality:

182   1st quality: events with at least four P-phases and clear arrival picks - 7326 events

183   2nd quality: events with pick residuals larger than ~2 s and greater location errors - 2944

184   events

185

186   ***Moment tensor inversions***

187   We selected aftershocks with M_L>4.5 to compute moment tensors from full waveform

188   inversions, including both body and surface waves. For this we used the software ISOLA

189   (Sokos and Zaharadnik, 2008) which can handle inversions of local to regional waveforms.

190   Green functions were computed using the 1-D model produced by León-Ríos et al. (2017)

191   and waveforms were inverted in the $10 - 25$ s period range. Horizontal centroid position was

192   kept fixed to the epicentral position from the earthquake locations, but a grid-search was

193   performed to obtain optimal centroid depth and time. Examples of the inversion and fitting

194   are provided in the Supplementary Material.

195

196   ***Magnitudes***

197   Local magnitudes (M_L) were calculated from maximum P-wave amplitudes on vertical

198   components. The obtained magnitudes vary between 0.7 and 6.9, with a magnitude of

199   completeness Mc=2.5 (Sup. Mat.). In general, there is a good agreement between the

200   calculated local magnitudes (M_L) and the moment magnitudes (Mw) obtained from our

201   moment tensor inversions and those from the GCMT catalogue (Sup. Mat.). Nonetheless, we

202   observe that for Mw>5.6 there is an underestimation of local magnitudes, probably due to

203   saturation of the M_L scale. On the other hand, for Mw<5.6 we observe an overestimation of

204   M_L by ~0.3 units. These differences are commonly observed when comparing local

205   magnitudes with moment magnitudes (e.g. Deichmann, 2006).

206

207   ***Residual bathymetry***

208   In order to compare the distribution of seismicity with the distribution of the incoming

209   oceanic relief, we produced a residual bathymetry grid for the Ecuadorian margin following

210   the ensemble averaging approach of Basset and Watts (2015), and using the higher resolution

211   GEBCO2014 grid. We calculated the average topography for a series of trench-normal

212   profiles. Then we subtracted this averaged topography from the original grid to produce an

213   elevation map where large-amplitude trench-normal variations associated with the subduction

214   zone have been removed and short-wavelength/lower amplitude structures are preserved and

215   highlighted.

216

217   **3. Spatio-temporal distribution of aftershocks**

218   Along strike, the aftershock seismicity extends beyond the coseismic rupture, over 300+ km,

219   from latitude 1°N to at least 1.5°S (Fig. 3). Along the dip direction, the seismicity seems to be

220   constrained by the coseismic rupture maximum depth, with most of the aftershocks located in

221   the upper 30 km and no aftershock seismicity locates deeper than the coseismic rupture

222   termination.

223

224   The most striking feature is the presence of three bands of seismicity perpendicular to the

225   trench, and located up-dip west of the mainshock rupture area (profiles BB', CC' and DD' in

226   Fig. 3; see also Soto-Cordero et al., 2017). Interestingly, this seismicity pattern is also

227   observed in the background seismicity during the interseismic period (Font et al., 2013). The

228   northern band (BB') extends for about 40 km up-dip with a width of about 10 km. The

229   central band (CC') is more diffuse, starting at the upper termination of the rupture area and

230   extending 40 km up-dip with a width of around 20 km. The southern band also starts at the

231   upper termination of the coseismic rupture and extends up-dip 60 km with a width of about

232   25 km. Both, the southern and central bands reach the trench, whilst seismicity is more

233   diffuse close to the trench for the northern band. Although we do observe seismicity near the

234   trench, we do not observe any extensional focal mechanism in this area that could be related

235   to outer rise seismicity following the mainshock (e.g. Sladen and Trevisan, 2018).

236   Considering the location uncertainties, most of the seismicity in these three alignments occurs

237   at the interface or within 10 km from it. Additionally, all large aftershocks (M>=5) occur

238   outside the mainshock rupture and mostly along bands BB' and DD', located up-dip at the

239   northern and southern limits of the co-seismic rupture, respectively. Inside the mainshock

240   rupture area, seismicity occurs mostly between the two patches of maximum coseismic slip

241   (Figure 5, see Section 5).

242

243   To the north (0.9° N), we observe a cluster of seismicity within the subduction interface

244   below the coastline (cluster G1 in Fig. 3). Further to the east, a cluster of crustal seismicity

245   (G2, hereafter called Esmeraldas sequence) is observed at 10-20 km depth. This group of

246   shallow seismicity started to develop at the end of June 2016, with a burst of seismicity

247   during July 5-8 and its largest earthquake, normal faulting Mw=4.9, occurring on July 6,

248   2016 (see details in Section 4).

249

250   South of the mainshock rupture area, we observe three separate groups of seismicity. The

251   first one is a cluster of events occurring beneath the coastline, at around latitude 0.9°S (G3).

252   This cluster seems to occur on the megathrust interface, and as seen in Section 4, presents

253   thrust focal mechanisms compatible with subduction earthquakes. The second group

254   corresponds to the seismicity observed inland at around latitude 1.3°S (G4) which also occur

255   at the interface. The third group (G5) is located offshore, nearby LPI. This seismicity is

256   sparsely distributed, and because of its location offshore at the southern end of the network, it

257   is difficult to assess hypocentral depths with certainty. Nevertheless, a clue regarding the

258   origin of this seismicity comes from previous studies which have found swarm-like

259   seismicity and SSEs in this area (Vallee et al., 2013; Segovia et al., 2018), as well as a SSE

260   during the early postseismic period of the 2016 mainshock (Rolandone et al., 2018). Like the

261   trench-normal bands, these three seismicity groups had also been observed during the

262   interseismic period (Segovia et al., 2018).

263

264   The spatio-temporal analysis of the aftershock sequence (Sup. Video) shows that during the

265   first 24 hours after the mainshock, aftershocks start to nucleate mostly along profiles DD' and

266   CC', and in particular between the two patches of maximum co-seismic slip. The aftershocks

267   then extend along profiles BB' and EE'. Seismicity around LPI starts on the third day with

268   peaks of activity on the 11th and 12th days after the mainshock. A last burst of seismicity in

269   this area occurs between 1st and 3rd December 2016. As stated above, the shallow clustered

270   seismicity of the Esmeraldas sequence occurs mostly during early July 2016. Finally, the

271   seismicity observed at the interface along the profile AA' develops during December 2016.

272

273   **4. Seismotectonics and moment tensor inversions**

274   For the 12-month period following the Pedernales mainshock (April 16 2016 – April 30

275   2017) there are 32 moment tensors with Mw between 4.8 and 6.9 available in the GCMT

276   catalogue (http://www.globalcmt.org/). We complemented these with 29 additional events

277   with Mw between 4.1 and 5.0, for a total of 61 moment tensors (Fig. 4 and Sup. Mat.). Most

278   of the moment tensors indicate thrust faulting at the subduction interface. No large

279   aftershocks (Mw>5) occur inside the coseismic rupture area. The largest thrust aftershocks

280   occur along the seismicity bands located at the northern and southern termination of the

281   mainshock rupture. Besides these two bands dominated by thrust faulting at the interface,

282   we also observe subduction earthquakes to the south, around latitude 1°S, and towards the

283   north by the coastline up to 1°N. The geometry of the reverse faulting focal mechanisms is

284   similar to that of the mainshock, with an average rotational angle (Kagan angle) of 22°

285   relative to the mainshock's focal mechanism (inset Fig. 4).

286

287   We also observe a few normal and strike-slip events. Strike-slip events seem to be sparsely

288   located and within the subducting slab. A possible explanation for this activity could be the

289   presence of pre-existing structures in the subducting CR, reactivated by the mainshock. On

290   the other hand, two similar normal fault earthquakes, of Mw 5.1 and 4.9 respectively,

291   occurred in the marine forearc around latitude 0.3°N, on June 1st 2016, separated by 5

292   hours. The GCMT centroid depths for these earthquakes (12 and 17 km depth) place them

293   close to the subduction interface, but on our own regional moment tensor inversions we

294   found the lowest waveform misfit at 5 km depth. Despite the depth uncertainties, a possible

295   explanation for this faulting could be given by the existence at this location of a subducted

296   seamount, previously imaged using multi-channel seismic reflection data (Marcaillou et al.,

297   2016). León-Ríos et al. (2017) hypothesize that the subduction of this structure produces an

298   anomalous extensional stress field parallel to the convergence vector, which in turn could

299   have been affected by the 2016 mainshock. In fact, Marcaillou et al. (2016) observed a

300   complex and highly fractured margin structure in this region, and argued that the absence

301   of background seismicity and low interseismic coupling here suggest that this area is

302 incapable of storing sufficient elastic strain to produce large thrust earthquakes and

303 tsunamis.

304

305 Two additional normal fault events are observed in our dataset. One is a Mw=4.4

306 intermediate-depth event, most likely intra-slab, located at 0.6°N, 200 km east of the

307 trench. The other is a Mw=4.9, crustal normal fault event with a strike-slip component,

308 belonging to the Esmeraldas sequence. Unfortunately, the uncertainties of our hypocentral

309 locations in this area do not allow us to distinguish the fault plane from the two nodal

310 planes. On the other hand, the geological map for this area (Reyes and Michaud, 2012; Sup.

311 Mat.) shows a set of normal faults striking ESE and dipping to the S, which coincide with one

312 of the nodal planes of this event (strike 103, dip 42, rake -29). We suggest that crustal

313 activity on one of these faults might be responsible for the seismicity observed during the

314 Esmeraldas sequence (see also Hoskins et al., 2018). Some previous large megathrust

315 aftershock sequences, such as Maule 2010 and Tohoku 2011, have shown similar shallow

316 normal faulting at the edges of the coseismic rupture area (e.g. Kato et al., 2011; Ryder et

317 al., 2012). A similar tectonic configuration could be responsible for our normal event in the

318 Esmeraldas area, which indicates horizontal extension in the overriding plate following the

319 mainshock. Since these events are shallow, near the coast, and can produce considerable

320 vertical displacement, they are important to consider when estimating earthquake and

321 tsunami hazard at a local scale.

322

323 ***The April 16 2016 Mw=4.9 foreshock***

324 Nearly 11 minutes before the Pedernales earthquake, an event M_W=4.9 nucleated about 14

325 km ESE of the mainshock's epicentre. We also obtained the moment tensor for this event,

326 which indicates a thrust faulting mechanism, likely on the subduction interface (Fig. 4). The

327 possibility of this earthquake to have triggered the Mw=7.8 mainshock is worth exploring,

328 although a dynamic or static triggering would be difficult to reconcile with the time and

329 distance between the two events. More accurate relocations of both the foreshock and main

330 event hypocentres, and a detailed analysis of the Coulomb stress change field, beyond the

331 scope of this study, would be necessary to resolve this issue.

332

333 **5. Relation between coseismic rupture and aftershock distribution**

334 As a first order feature, we observe an inverse correlation between the number of aftershocks

335 and co-seismic slip, with highs in slip associated to lows in seismicity and vice versa (e.g. at

336 20, 45 and 60 km south of the mainshock in profile N-S of Fig. 3). Figure 5 shows in detail

337 the distribution of aftershocks and co-seismic slip. We observe that most of the large

338 aftershocks occur outside the mainshock rupture area (defined as the 1 m slip contour area).

339 When we consider all magnitudes, 28% of the aftershocks occur inside the mainshock

340 rupture, but when we consider only events with $M_L \geq 3.5$, only 14% of aftershocks nucleate

341 inside and, moreover, no aftershock larger than $M_L=5$ nucleated inside the mainshock rupture

342 area.

343

344 Additionally, the histograms in Fig. 5 show the normalized areal distribution of co-seismic

345 slip together with the normalized frequency distribution of aftershocks inside the coseismic

346 rupture. Accordingly, if the aftershocks occurrence were randomly distributed, the aftershock

347 frequency curve would resemble the slip frequency distribution. Instead, we observe that

348 aftershocks tend to concentrate at intermediate levels of coseismic slip (2 - 3.5 m),

349 particularly in areas of large slip gradient, such as in between the two patches of coseismic

350 slip maxima. On the other hand, areas of low coseismic slip (< 2 m) present less seismicity

351 than expected, whilst areas of high coseismic slip (> 4.5 m) seem to present a random

352 distribution of aftershocks (histogram Fig. 5a), although when we consider only events with

353 $M_L \geq 3.5$, there is a lack of aftershocks compared to a random distribution (histogram Fig. 5b).

354

355 If we look at the aftershock density, we observe that in terms of number of events, the highest

356 density is located inside the mainshock rupture area, in between the two patches of maximum

357 coseismic slip (Fig. 6a). If instead we look at the seismic moment density (Fig. 6b), we

358 observe that inside the mainshock rupture area the moment density is relatively low ($< 1e^{17}$ N

359 m / 0.1°x0.1°). On the other hand, high moment density ($> 1e^{18}$ N m / 0.1°x0.1°) is observed

360 outside the mainshock rupture, along the three trench-normal seismicity bands and

361 particularly nearby the coastline at latitude 0.5°N, due to the occurrence here of the largest

362 aftershock of the sequence (Mw=6.9, thrust faulting).

363

364 **6. Relation between seismic and aseismic processes**

365 We compare the temporal evolution of the aftershock sequence with that of the geodetic

366 afterslip during the first 30 days following the mainshock. Following Rolandone et al. (2018),

367 we consider the afterslip and aftershocks as three discrete patches (North, South and LPI; see

368 Fig. 3 and Sup. Mat) according to their spatial distribution, and analyse them separately (Fig.

369 7). Cumulative seismicity (red curve) for the northern and southern patches show an Omori-

370 type decay in which a steep slope is observed immediately after the mainshock, followed by a

371 deceleration after the first week of aftershocks. On the other hand, the LPI patch shows a

372 rather slow start in aftershocks generation, and then an increase from day 8 until day ~20

373 when it decreases again. The different behaviour in the LPI patch could be explained because

374 this area hosted a slow slip event associated to seismicity during this period (Rolandone et al.,

375 2018).

376   We observe for all three patches that the curve for cumulative number of earthquakes closely

377   follows that of the afterslip cumulative moment release, implying a linear relationship

378   between both processes. In fact, if we assume that both afterslip and aftershocks cumulative

379   distributions present an exponential behaviour, their curves should resemble a straight-line in

380   a semi-logarithmic plot, as seen in the right panels of Fig. 7, which also show both curves

381   present similar slopes (segmented lines). Leaving the LPI patch aside, the linear relation

382   between cumulative aftershocks and afterslip release is remarkable.

383

384   Furthermore, for each of the patches we observe that after 30 days of postseismic activity, the

385   total cumulative moment released by the aftershocks represents about 10% of the cumulative

386   moment released by the afterslip, indicating that most of the postseismic deformation is

387   aseismic (Sup. Mat).

388

389   Additionally, we explore the spatial dependency between afterslip and aftershocks. As seen

390   from the geographic distribution of seismicity outside the mainshock rupture area,

391   aftershocks are spatially associated with afterslip, particularly in the area of the trench-normal

392   bands and around LPI (Fig. 3). Figure 8 shows the temporal evolution of seismicity as a

393   function of along-strike distance from the mainshock epicentre, clearly showing a log-time

394   expansion of the aftershocks. A similar behaviour is seen for the along-dip direction (Sup.

395   Mat). These observations are consistent with previous studies (e.g. Frank et al., 2017), and

396   numerical modelling (e.g. Ariyoshi et al., 2007; Perfettini et al., 2018) which suggest that this

397   type of semilogarithmic migration is indicative of afterslip-driven aftershock activity.

398

399

400

7. Discussion

7.1 Where do aftershocks occur?

The largest aftershocks occur outside the mainshock rupture area. This finding is in agreement with previous studies which have found that regions of high coseismic slip are mostly devoid of large aftershocks, whilst post-seismic seismicity tends to concentrate at the edges of the coseismic rupture (e.g. Das and Henry, 2003; Asano et al., 2011; Rietbrock et al., 2012; Agurto et al., 2012; Frank at al., 2017; Wetzler et al., 2018). For the 2010 Mw=8.8 Maule earthquake, Agurto et al. (2012) also found that aftershocks concentrated at intermediate levels of coseismic slip, with areas of low and large coseismic slip lacking in aftershocks. Therefore, this could be a common feature for large megathrust earthquakes with a heterogeneous distribution of coseismic slip.

Additionally, a large number of aftershocks do occur within the co-seismic rupture area, although presenting low magnitudes. The fact that aftershocks nucleate inside the mainshock rupture area indicates that the accumulated strain energy within the fault is not totally released during the mainshock, or at least that this release is not homogeneously distributed along the megathrust rupture. Attempting to investigate this issue, Yabe and Ide (2018) produced quasi-dynamic numerical simulations in which they replicate several megathrust frictional scenarios and mainshock ruptures with their respective aftershock sequences. They observed aftershocks around and within the mainshock rupture area for cases in which frictional heterogeneity varies significantly along the fault. On the other hand, aftershocks were not produced when frictional heterogeneities along the fault were small. Similarly, the fact that for the Pedernales sequence we observe the highest density of aftershocks within the mainshock rupture area, might be indicative of the highly heterogeneous distribution of frictional properties along the northern Ecuador megathrust.

426 When we account for location uncertainties, the low-magnitude seismicity located within the

427 co-seismic rupture area seems to occur distributed within the seismogenic volume and not

428 only at the megathrust interface (Fig. 3). This volume represents the off-fault damage zone

429 produced by successive megathrust ruptures, and it usually concentrates a diversity of

430 aftershocks focal mechanisms in structures re-activated by the mainshock (e.g. Asano et al.,

431 2011; Agurto et al., 2012).

432

433 *7.2 What controls the evolution of the aftershock seismicity?*

434 The temporal linear dependency between afterslip and aftershocks shown here (Fig. 7)

435 suggests a causative time-based relationship between these two processes, and therefore the

436 temporal distribution of aftershocks associated to patches of afterslip would be modulated by

437 the stressing rate associated with afterslip (e.g. Perfettini and Avouac, 2004; Hsu et al.,

438 2006).

439

440 Additionally, the semi-logarithmic migration of aftershocks both along strike and dip (Fig. 8)

441 suggests that afterslip also controls the spatial extension and migration speed of aftershocks

442 (e.g. Frank et al., 2017; Perfettini et al., 2018). We notice that the origin of the two red lines

443 indicating the propagation front in Fig. 8 is not located at the epicentre but approximately 40

444 km south of it, in the area where most of the aftershock seismicity take place during the first

445 24 hours following the mainshock (Section 3). This corresponds to the centre of the

446 coseismic rupture, and therefore we hypothesize that the expansion of aftershocks is initiated

447 at this point, subsequently propagating outwards.

448

449 Another explanation for the observed aftershocks expansion could be related to fluid

450 diffusion. Nevertheless, in such a case we would observe that the distance D associated with

451 the migration front of the seismicity is related to time t as D~sqrt(t)c, where c is the hydraulic

452 diffusivity coefficient (Wang, 2000). This is unlike our observations, in which we see that

453 D~log(t).

454

455 Finally, we notice that a similar relationship between seismic and aseismic processes in our

456 study area has also been described during the interseismic period (Vallée et al., 2013;

457 Rolandone et al., 2018; Segovia et al., 2018; Vaca et al., 2018). These previous studies

458 describe seismic swarms associated to SSEs in the offshore area in front of Punta Galera (lat.

459 ~0.7°N; Vaca et al., 2018), and around LPI (Vallée et al., 2013; Segovia et al., 2018). A

460 similar SSE around LPI occurred during the postseismic period of the 2016 Pedernales

461 earthquake, also associated with seismicity (Rolandone et al., 2018). Therefore, it seems that

462 the close spatio-temporal correlation between seismic and aseismic processes in this region is

463 persistent during the whole of the earthquake cycle.

464

465 *7.3 Persistent seismicity patterns over the earthquake cycle*

466 Aseismic slip seems to modulate the rate and spatio-temporal expansion of the aftershock

467 seismicity. But why do these slip processes occur where they occur in the first place? In our

468 study area, the presence of persistent spatial seismicity patterns over the earthquake cycle,

469 such as the three trench-normal bands and the seismicity south of the mainshock rupture area

470 (Font et al., 2013), suggest that earthquake nucleation in these areas is somehow controlled

471 by long-lived structural features. We also notice that the bands are dominated by thrust events

472 (Fig. 4), and oriented perpendicular to the trench, similar to the slip vector of the mainshock,

473 as opposed to parallel to the convergence vector.

474

475   To our knowledge, no other subduction zone presents this type of permanent seismicity

476   pattern transcending the earthquake cycle. Observations in other tectonic settings such as

477   Parkfield, in the San Andreas fault, show sub-horizontal alignments of seismicity along the

478   fault plane that also persist through many seismic cycles. Because of its geometry and the

479   motion of the fault, it has been proposed that this seismic activity is related to rheological

480   transitions within the fault zone and/or stress concentrations between locked and creeping

481   areas (e.g. *Waldhauser et al.*, 2004). Nonetheless, invoking rheological transitions in our area

482   is a less plausible hypothesis to explain our observations, mainly because the seismicity

483   within the bands lacks any clear depth-dependency.

484

485   One additional hypothesis is that the interface frictional properties in these regions of high

486   seismicity are somehow different than in the rest of the area. In this sense, the interseismic

487   coupling map for our study region (Fig. 1) shows that the general area of the bands is only

488   slightly coupled (<40%), but the model lacks the resolution to see any difference along strike,

489   between areas with seismicity (bands) and areas without.

490

491   *7.4 Influence of the subducting seafloor relief*

492   Previous studies have proposed an along-strike segmentation of the Ecuadorian margin in

493   which large subduction earthquakes only occur north of the CR, which acts as a barrier to the

494   southward propagation of megathrust ruptures (e.g. Collot et al., 2004). More generally, it has

495   been proposed that rugged subducting seafloor, as in the case of seamounts and ridges, give

496   rise to heterogeneous stresses, promoting creep as expressed in transient events of various

497   spatial and temporal scales, accompanied with small and medium-sized earthquakes (Wang

498   and Bilek, 2014). Bassett and Watts (2015) produced a compilation of residual bathymetric

499   anomalies for several subduction zones of the world, and found that regions with subducted

500   seamounts were correlated to reduced levels of megathrust activity, suggesting that these

501   areas are mostly associated with small earthquakes and creep rather than with large

502   megathrust events. Furthermore, they argue that larger bathymetric features, such as aseismic

503   ridges, exhibit seafloor roughness over a larger scale than subducted seamounts, presenting

504   widths comparable to the rupture length of large (Mw~7) megathrust earthquakes. They

505   observe that the maximum roughness is located at the flanks of the ridges, which often serve

506   as barriers of rupture propagation. For the Ecuador subduction zone, some authors observed

507   that the northern flank of the CR has acted as a barrier against the southward propagation of

508   the 1906 and 1942 earthquakes (Kelleher, 1972; Collot et al., 2004).

509

510   Following the ensemble averaging approach of Bassett and Watts (2015), and benefiting from

511   combined high resolution datasets, we produced improved maps of residual bathymetry for

512   the Ecuadorian margin. We compared the spatial distribution of these anomalies with the

513   distribution of the seismic and aseismic processes before and after the Pedernales earthquake

514   (Fig. 9). Landward from the trench, the down-dip limit of the area with high residual

515   bathymetry (>2 km) coincides with the up-dip limit of the Pedernales earthquake rupture

516   area. Bassett and Watts (2015) notice that this limit coincide with the continental slope break,

517   and suggest that the slope break corresponds to the updip limit of the seismogenic zone, and

518   that the outer portion of the plate interface, below the steep continental slope, is

519   weak/conditionally stable and would slip aseismically. Furthermore, we notice that both the

520   1942 and the 2016 epicentres are located nearby this limit, with the 2016 mainshock rupture

521   area itself extending down-dip from this limit, within an area of smoother residual

522   bathymetry. We also notice that the trench-normal bands of seismicity observed during the

523   interseismic and post-seismic periods occur in areas of higher gradient and residual

524   bathymetry. In particular, the seismicity band DD', which marks the southern boundary of

525   the Pedernales rupture zone, is in front of the highest bathymetric and gravity anomaly,

526   which correspond to the thickest part of the CR crust (~20 km; Collot et al., 2004; Sallarès et

527   al., 2005). Lastly, both the SSEs observed during the interseismic period, and the afterslip

528   patches observed during the post-seismic period occur in areas dominated by high residual

529   bathymetry due to the subduction of the CR (Fig. 9).

530

531   We summarize our observations in an interpretative figure (Fig. 10) in which we suggest that

532   the Ecuadorian margin hosts a bimodal slip mode mechanically controlled by the distribution

533   of the subducting oceanic relief. The bimodal slip mode produces seismic and aseismic slip

534   processes, and is present both along-strike and along-dip. In the area where the CR subducts

535   beneath the margin (latitude 0° to ~2.5°S), particularly in the region containing a high

536   residual bathymetry (>2 km, from the trench until ~90 km landward; Zone A in Fig. 10), the

537   overall ISC is low (<40%), and the subduction slip mode is dominated by creep and small to

538   medium-sized earthquakes (Mw<6), swarm-like seismicity and SSEs during the interseismic

539   phase, and aseismic afterslip during the postseismic period. Down-dip of this limit (i.e. over

540   90 km horizontally from the trench, down to the maximum seismogenic depth; Zone B), the

541   ISC is higher (>40%) and the slip mode is dominated by large subduction earthquakes

542   (Mw>7) as in the case of the 2016 Pedernales Earthquake and similar past ruptures. Along

543   strike to the north of the ridge flank, away from the area of influence of the CR (Zone C), the

544   overall ISC is high up to the trench, and megathrust earthquake ruptures could reach the

545   trench, as allegedly was the case for the 1906 earthquake and possibly the 1979 earthquake.

546   Therefore, Zone A presents an overall stable regime (velocity-strengthening) whilst Zones B

547   and C are unstable/conditionally stable (velocity-weakening). Thus, the area of high residual

548   bathymetry (> 2 km) would act as a barrier to up-dip (trench-normal) propagation of

549 megathrust ruptures, whilst the lateral flanks of the ridge would act as barriers to along-strike

550 (trench-parallel) rupture propagation.

551

552 **8. Conclusion**

553 We characterised the aftershock seismicity occurring in the Ecuadorian margin over one year

554 following the 2016 Mw=7.8 Pedernales earthquake. More than 10,000 events were detected

555 and located, with magnitudes up to 6.9. Most of the seismicity results from interplate thrust

556 faulting but we also observe a few normal and strike-slip mechanisms. Within the mainshock

557 rupture area, seismicity concentrates in regions of intermediate coseismic slip, particularly in

558 between the two patches of slip maxima. Outside the rupture area, seismicity extends for

559 more than 300 km along strike. The most striking feature is the presence of three seismicity

560 bands, perpendicular to the trench, which are also observed during the interseismic period.

561

562 We observe a linear dependency between the temporal evolution of afterslip and number of

563 aftershocks, confirming previous results (Rolandone et al., 2018). Additionally, aftershocks

564 present a temporal semi-logarithmic expansion along the strike and dip directions, which

565 further suggest their spatio-temporal occurrence is regulated by afterslip. A comparison of the

566 distribution of seismic and aseismic slip processes with the distribution of bathymetric

567 anomalies reveals that slip in the area seems to be controlled by the subduction of oceanic

568 plate roughness. To explain our observations, we propose a conceptual model in which the

569 Ecuadorian margin presents a bimodal slip mode mechanically controlled by the subduction

570 of a rough oceanic relief. In this sense, the flanks of the CR act as a barrier to the propagation

571 of megathrust ruptures, both up-dip and along-strike. On the other hand, the area of

572 maximum influence of the CR (residual bathymetry > 2 km) is characterized by small

573 magnitude earthquakes (Mw<6), aseismic slip, repeating events and earthquake swarms.

References

Agurto, H., Rietbrock, A., Ryder, I., Miller, M., 2012. Seismic-afterslip characterization of the 2010 Mw 8.8 Maule, Chile, earthquake based on moment tensor inversion. Geophys. Res. Lett. 39. https://doi.org/10.1029/2012GL053434

Alvarado, A., Ruiz, M., Mothes, P., Yepes, H., Segovia, M., Vaca, M., Ramos, C., Enríquez, W., Ponce, G., Jarrín, P., Aguilar, J., Acero, W., Vaca, S., Singaucho, J.C., Pacheco, D., Córdova, A., 2018. Seismic, Volcanic, and Geodetic Networks in Ecuador: Building Capacity for Monitoring and Research. Seismol. Res. Lett. 89. https://doi.org/10.1785/0220170229

Ariyoshi, K., Matsuzawa, T., Hasegawa, A., 2007. The key frictional parameters controlling spatial variations in the speed of postseismic-slip propagation on a subduction plate boundary. Earth Planet. Sci. Lett. 256, 136–146. https://doi.org/10.1016/j.epsl.2007.01.019

Asano, Y., Saito, T., Ito, Y., Shiomi, K., Hirose, H., Matsumoto, T., Aoi, S., Hori, S., Sekiguchi, S., 2011. Spatial distribution and focal mechanisms of aftershocks of the 2011 off the Pacific coast of Tohoku Earthquake. Earth, Planets Sp. 63, 669–673. https://doi.org/10.5047/eps.2011.06.016

Basset, D., Watts, A., 2015. Gravity anomalies, crustal structure, and seismicity at subduction zones: 1. Seafloor roughness and subducting relief. Geochemistry Geophys. Geosystems 16, 1508–1540. https://doi.org/10.1002/ 2014GC005684

Beck, S.L., Ruff, L.J., 1984. The rupture process of the great 1979 Colombia earthquake: evidence for the asperity model. J. Geophys. Res. 89, 9281–9291. https://doi.org/10.1029/JB089iB11p09281

618 Beck, S.L., Rietbrock, A., Tilmann, F., Barrientos, S., Meltzer, A.S., Oncken, O., Bataille,
619   K., Roeker, S., Vilotte, J.-P., Russo, R.M., 2014. Advancing Subduction Zone Science
620   After a Big Quake Access and Use of Data Lead to Innovative Ways. EOS, Trans. Am.
621   Geophys. Union 95, 193–194.

622 Bilek, S.L., Lay, T., 2018. Subduction zone megathrust earthquakes. Geosphere 14, 1–33.
623   https://doi.org/10.1130/GES01608.1

624 Chlieh, M., Mothes, P.A., Nocquet, J.M., Jarrin, P., Charvis, P., Cisneros, D., Font, Y.,
625   Collot, J.Y., Villegas-Lanza, J.C., Rolandone, F., Vallée, M., Regnier, M., Segovia, M.,
626   Martin, X., Yepes, H., 2014. Distribution of discrete seismic asperities and aseismic slip
627   along the Ecuadorian megathrust. Earth Planet. Sci. Lett. 400, 292–301.
628   https://doi.org/10.1016/j.epsl.2014.05.027

629 Collot, J.Y., Marcaillou, B., Sage, F., Michaud, F., Agudelo, W., Charvis, P., Graindorge, D.,
630   Gutscher, M.A., Spence, G., 2004. Are rupture zone limits of great subduction
631   earthquakes controlled by upper plate structures? Evidence from multichannel seismic
632   reflection data acquired across the northern Ecuador-southwest Colombia margin. J.
633   Geophys. Res. Solid Earth 109, 1–14. https://doi.org/10.1029/2004JB003060

634 Das, S., Henry, C., 2003. Spatial relation between main earthquake slip and its aftershock
635   distribution. Rev. Geophys. 41. https://doi.org/10.1029/2002RG000119

636 Deichmann, N., 2006. Local Magnitude, a Moment Revisited. Bull. Seismol. Soc. Am. 96,
637   1267–1277. https://doi.org/10.1785/0120050115

638 Ester, M., Kriegel, H., Sander, J., Xu, X., 1996. A Density-Based Algorithm for Discovering
639   Clusters in Large Spatial Databases with Noise. KDD 96, 226–231.

640 Font, Y., Segovia, M., Vaca, S., Theunissen, T., 2013. Seismicity patterns along the
641   ecuadorian subduction zone: New constraints from earthquake location in a 3-D a priori
642   velocity model. Geophys. J. Int. 193, 263–286. https://doi.org/10.1093/gji/ggs083

643 Frank, W.B., Poli, P., Perfettini, H., 2017. Mapping the rheology of the Central Chile
644   subduction zone with aftershocks. Geophys. Res. Lett. 44, 5374–5382.
645   https://doi.org/10.1002/2016GL072288

646 Freed, A.M., 2005. Earthquake Triggering By Static, Dynamic, and Postseismic Stress
647   Transfer. Annu. Rev. Earth Planet. Sci. 33, 335–367.
648   https://doi.org/10.1146/annurev.earth.33.092203.122505

649 Gombert, B., Duputel, Z., Jolivet, R., Simons, M., Jiang, J., Liang, C., Fielding, E.J., Rivera,
650   L., 2018. Strain budget of the Ecuador–Colombia subduction zone: A stochastic view.
651   Earth Planet. Sci. Lett. 498, 288–299. https://doi.org/10.1016/j.epsl.2018.06.046

652 Hardebeck, J.L., 2012. Coseismic and postseismic stress rotations due to great subduction
653   zone earthquakes. Geophys. Res. Lett. 39, 1–6. https://doi.org/10.1029/2012GL053438

654 Hoskins, M., Meltzer, A., Soto-Cordero, L., Stachnik, J., Beck, S., Lynner, C., Ruiz., M.C.,
655   Alvarado, A., Hernandez, S., Charvis, P., Font, Y., Nocquet, J.M., Rolandone, F.,

656   Regnier, M., Agurto-Detzel, H., León-Ríos, S., Rietbrock, A., 2018. Variable Slip
657   Modes in Postseismic Deformation North of the April 16, 2016 M_w 7.8 Pedernales,
658   Ecuador Megathrust Earthquake. Abstract T43E-0444 *2018 Fall Meeting, AGU*,
659   Washington, D.C., 10-14 Dec.

660   Hsu, Y.J., Simons, M., Avouac, J.P., Galeteka, J., Sieh, K., Chlieh, M., Natawidjaja, D.,
661   Prawirodirdjo, L., Bock, Y., 2006. Frictional afterslip following the 2005 Nias-Simeulue
662   earthquake, Sumatra. Science (80-.). 312, 1921–1926.
663   https://doi.org/10.1126/science.1126960

664   Kanamori, H., McNally, K.C., 1982. Variable rupture mode of the subduction zone along the
665   Ecuador-Colombia coast. Bull. Seismol. Soc. Am. 72, 1241–1253.

666   Kato, A., Sakai, S., Obara, K., 2011. A normal-faulting seismic sequence triggered by the
667   2011 off the Pacific coast of Tohoku Earthquake: Wholesale stress regime changes in
668   the upper plate. Earth, Planets Sp. 63, 745–748. https://doi.org/10.5047/eps.2011.06.014

669   Kelleher, J.A.., 1972. Rupture zones of large South American earthquakes and some
670   predictions. J. Geophys. Res. 77, 2087. https://doi.org/10.1029/JB077i011p02087

671   Leon-Rios, S., Aguiar, A.L., Bie, L., Edwards, B., Velasco, A.J.F., Holt, J., Garth, T.,
672   González, P.J., Rietbrock, A., Agurto-Detzel, H., Charvis, P., Font, Y., Nocquet, J.M.,
673   Regnier, M., Renouard, A., Mercerat, D., Permoud, M., Beck., S., Meltzer., A., Soto-
674   Cordero., L., Alvarado., A., Perrault, M., Ruiz, M. and Santo, J., 2017. The 2016 Mw
675   7.8 Pedernales, Ecuador earthquake: Minimum 1D Velocity Model and Regional
676   Moment Tensors Based on the Aftershock Sequence. Abstract S53C-2352 presented at
677   *2017 Fall Meeting, AGU*, New Orleans, LA, 11-15 Dec.

678   Lomax, A., Virieux, J., Volant, P., Berge-Thierry, C., 2000. Probabilistic Earthquake
679   Location in 3D and Layered Models, in: Thurber, C.H., Rabinowitz, N. (Eds.),
680   Advances in Seismic Event Location. Kluwer Academic Publishers, pp. 101–134.
681   https://doi.org/10.1007/978-94-015-9536-0_5

682   Marcaillou, B., Collot, J.Y., Ribodetti, A., d'Acremont, E., Mahamat, A.A., Alvarado, A.,
683   2016. Seamount subduction at the North-Ecuadorian convergent margin: Effects on
684   structures, inter-seismic coupling and seismogenesis. Earth Planet. Sci. Lett. 433, 146–
685   158. https://doi.org/10.1016/j.epsl.2015.10.043

686   Meltzer A., S. Beck, M. Ruiz, M. Hoskins, L. Soto-Cordero, J.C. Stachnik, C. Lynner, R.
687   Porritt, D. Portner, A. Alvarado, S. Hernandez, H. Yepes, P. Charvis, Y. Font, M.
688   Regnier, A. Rietbrock, 2018. The 2016 Mw 7.8 Pedernales Earthquake, Ecuador:
689   RAPID Response Deployment. *Submitted*.

690   Nocquet, J.M., Jarrin, P., Vallée, M., Mothes, P.A., Grandin, R., Rolandone, F., Delouis, B.,
691   Yepes, H., Font, Y., Fuentes, D., Régnier, M., Laurendeau, A., Cisneros, D., Hernandez,
692   S., Sladen, A., Singaucho, J.C., Mora, H., Gomez, J., Montes, L., Charvis, P., 2017.
693   Supercycle at the Ecuadorian subduction zone revealed after the 2016 Pedernales
694   earthquake. Nat. Geosci. 10, 145–149. https://doi.org/10.1038/ngeo2864

695 Nocquet, J.M., Villegas-Lanza, J.C., Chlieh, M., Mothes, P.A., Rolandone, F., Jarrin, P.,
696   Cisneros, D., Alvarado, A., Audin, L., Bondoux, F., Martin, X., Font, Y., Régnier, M.,
697   Vallée, M., Tran, T., Beauval, C., Maguiña Mendoza, J.M., Martinez, W., Tavera, H.,
698   Yepes, H., 2014. Motion of continental slivers and creeping subduction in the northern
699   Andes. Nat. Geosci. 7, 287–291. https://doi.org/10.1038/ngeo2099

700 Perfettini, H., Avouac, J., 2004. Postseismic relaxation driven by brittle creep: A possible
701   mechanism to reconcile geodetic measurements and the decay rate of aftershocks,
702   application to the Chi-Chi earthquake, Taiwan 109, 1–15.
703   https://doi.org/10.1029/2003JB002488

704 Perfettini, H., Frank, W.B., Marsan, D., Bouchon, M., 2018. A Model of Aftershock
705   Migration Driven by Afterslip. Geophys. Res. Lett. 45, 2283–2293.
706   https://doi.org/10.1002/2017GL076287

707 Reyes, P., Michaud, F., 2012. Mapa Geológico de la Margen Costera Ecuatoriana (1:50000).
708   EP PetroEcuador, Quito, Ecuador.

709 Rietbrock, A., Ryder, I., Hayes, G., Haberland, C., Comte, D., Roecker, S., Lyon-Caen, H.,
710   2012. Aftershock seismicity of the 2010 Maule Mw=8.8, Chile, earthquake: Correlation
711   between co-seismic slip models and aftershock distribution? Geophys. Res. Lett. 39, 2–
712   6. https://doi.org/10.1029/2012GL051308

713 Rolandone, F., Nocquet, J.M., Mothes, P.A., Jarrin, P., Vallée, M., Cubas, N., Hernandez, S.,
714   Plain, M., Vaca, S., Font, Y., 2018. Areas prone to slow slip events impede earthquake
715   rupture propagation and promote afterslip. Sci. Adv. 4, 2–9.
716   https://doi.org/10.1126/sciadv.aao6596

717 Ryder, I., Rietbrock, A., Kelson, K., Bürgmann, R., Floyd, M., Socquet, A., Vigny, C.,
718   Carrizo, D., 2012. Large extensional aftershocks in the continental forearc triggered by
719   the 2010 Maule earthquake, Chile. Geophys. J. Int. 188, 879–890.
720   https://doi.org/10.1111/j.1365-246X.2011.05321.x

721 Sallarès, V., Charvis, P., Flueh, E.R., Bialas, J., Party, S.S., 2005. Seismic structure of the
722   Carnegie ridge and the nature of the Galápagos ho. Geophys. J. Int. 161, 763–788.
723   https://doi.org/10.1111/j.1365-246X.2005.02592.x

724 Segovia, M., Font, Y., Régnier, M., Charvis, P., Galve, A., 2018. Seismicity Distribution
725   Near a Subducting Seamount in the Central Ecuadorian Subduction Zone, Space-Time
726   Relation to a Slow-Slip Event. Tectonics 37, 2106–2123.
727   https://doi.org/10.1029/2017TC004771

728 Sladen, A., Trevisan, J., 2018. Shallow megathrust earthquake ruptures betrayed by their
729   outer-trench aftershocks signature. Earth Planet. Sci. Lett. 483, 105–113.
730   https://doi.org/10.1016/j.epsl.2017.12.006

731 Sokos, E.N., Zahradnik, J., 2008. ISOLA a Fortran code and a Matlab GUI to perform
732   multiple-point source inversion of seismic data. Comput. Geosci. 34, 967–977.
733   https://doi.org/10.1016/j.cageo.2007.07.005

734 Soto-Cordero L., J. Nealy, A. Meltzer, H. Agurto-Detzel. A. Alvarado, S. Beck, H. Benz, E.
735   Bergman, P. Charvis, Y. Font, G. Hayes, S. Hernandez, M. Hoskins, S. Leon Rios, C.
736   Lynner, M. Regnier, A. Rietbrock, M. Ruiz, J. C. Stachnik, W. Yeck, 2017, New
737   insights on co- and post-seismic deformation and slip behavior associated with the
738   Mw7.8 2016 Pedernales, Ecuador earthquake and its aftershock sequence", Abstract
739   S53C-0715 presented at *2017 Fall Meeting, AGU*, New Orleans, LA, 11-15 Dec

740 Stein, R.S., 1999. The role of stress transfer in earthquake occurrence : Abstract : Nature.
741   Nature 402, 605–609.

742 Vaca, S., Vallée, M., Nocquet, J.M., Battaglia, J., Régnier, M., 2018. Recurrent slow slip
743   events as a barrier to the northward rupture propagation of the 2016 Pedernales
744   earthquake (Central Ecuador). Tectonophysics 724–725, 80–92.
745   https://doi.org/10.1016/j.tecto.2017.12.012

746 Vallée, M., Nocquet, J.M., Battaglia, J., Font, Y., Segovia, M., Régnier, M., Mothes, P.,
747   Jarrin, P., Cisneros, D., Vaca, S., Yepes, H., Martin, X., Béthoux, N., Chlieh, M., 2013.
748   Intense interface seismicity triggered by a shallow slow slip event in the Central
749   Ecuador subduction zone. J. Geophys. Res. Solid Earth 118, 2965–2981.
750   https://doi.org/10.1002/jgrb.50216

751 Waldhauser, F., Ellsworth, W.L., Schaff, D.P., Cole, A., 2004. Streaks, multiplets, and holes:
752   High-resolution spatio-temporal behavior of Parkfield seismicity. Geophys. Res. Lett.
753   31, L18608. https://doi.org/10.1029/2004GL020649

754 Wang, H.F., 2000. Theory of Linear Poroelasticity. Princeton Univ. Press., Princeton, N.J.

755 Wang, K., Bilek, S.L., 2014. Invited review paper: Fault creep caused by subduction of rough
756   seafloor relief. Tectonophysics 610, 1–24. https://doi.org/10.1016/j.tecto.2013.11.024

757 Wessel, P., Smith, W.H.F., 1998. New, improved version of generic mapping tools released.
758   Eos, Trans. Am. Geophys. Union 79, 579–579. https://doi.org/10.1029/98EO00426

759 Wetzler, N., Lay, T., Brodsky, E.E., Kanamori, H., 2018. Systematic deficiency of
760   aftershocks in areas of high coseismic slip for large subduction zone earthquakes. Sci.
761   Adv. 4, 1–9. https://doi.org/10.1126/sciadv.aao3225

762 Yabe, S., Ide, S., 2018. Why Do Aftershocks Occur Within the Rupture Area of a Large
763   Earthquake? Geophys. Res. Lett. 45, 4780–4787.
764   https://doi.org/10.1029/2018GL077843

765 Ye, L., Kanamori, H., Avouac, J.P., Li, L., Cheung, K.F., Lay, T., 2016. The 16 April 2016,
766   MW7.8 (MS7.5) Ecuador earthquake: A quasi-repeat of the 1942 MS7.5 earthquake and
767   partial re-rupture of the 1906 MS8.6 Colombia–Ecuador earthquake. Earth Planet. Sci.
768   Lett. 454, 248–258. https://doi.org/10.1016/j.epsl.2016.09.006

769 Yoshimoto, M., Kumagai, H., Acero, W., Ponce, G., Vásconez, F., Arrais, S., Ruiz, M.,
770   Alvarado, A., Pedraza García, P., Dionicio, V., Chamorro, O., Maeda, Y., Nakano, M.,
771   2017. Depth-dependent rupture mode along the Ecuador-Colombia subduction zone.
772   Geophys. Res. Lett. 44, 2203–2210. https://doi.org/10.1002/2016GL071929
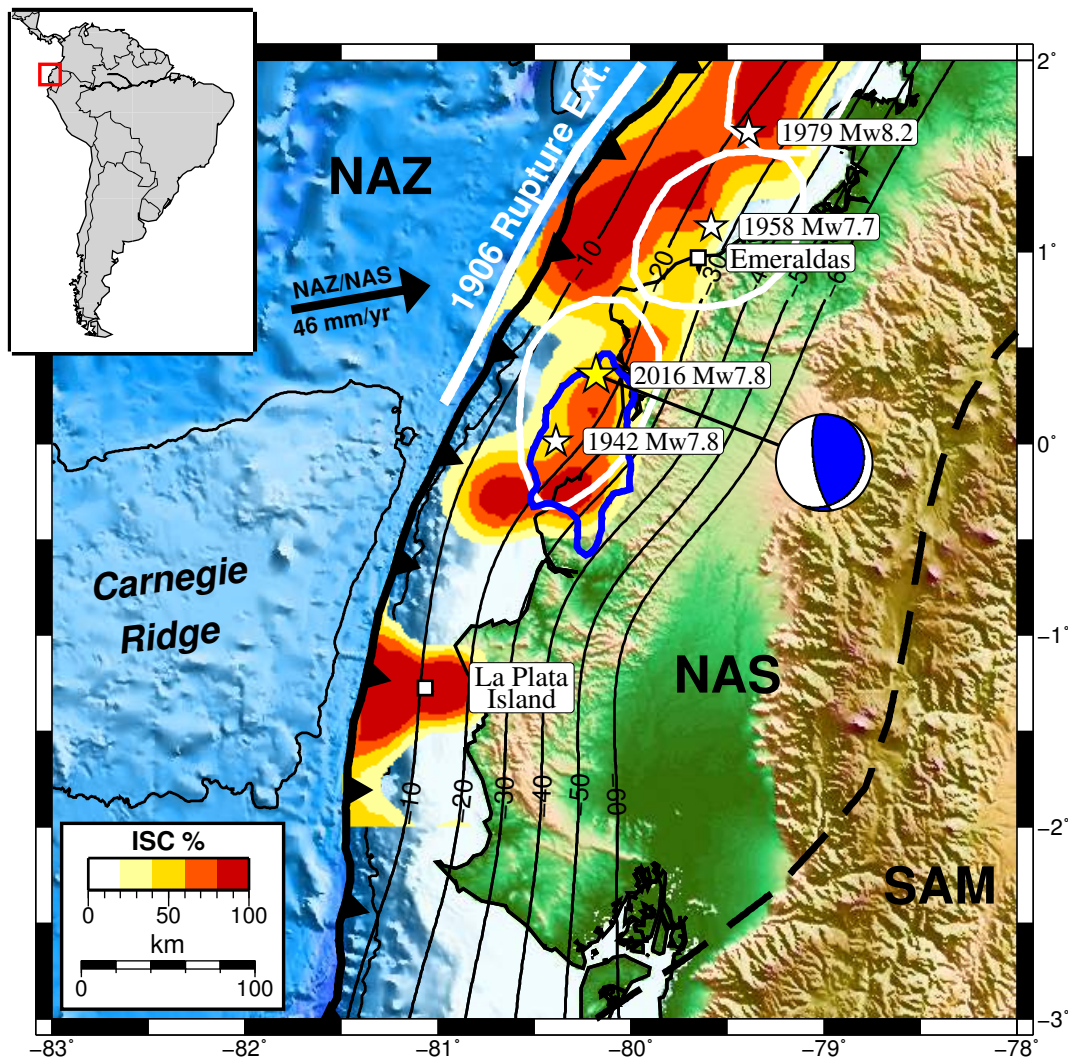
Figure 1. Interseismic coupling (Nocquet et al., 2014) and main seismotectonic features.
White stars and solid white lines show epicentres and approximate rupture areas of past
megathrust earthquakes respectively (Kanamori and McNally, 1982; Mendoza and Dewey,
1984). Yellow star shows epicentre of 2016 mainshock together with its GCMT focal
mechanism. Blue contour shows rupture area of 2016 event (Nocquet et al., 2017). Black
contours show depth of subduction interface every 10 km (Hayes, 2012). Segmented black
line indicates the Dolores-Guayaquil Fault Zone (Collot et al., 2002). Convergence
NAZ/NAS from Chlieh et al. (2014). NAZ Nazca Plate, NAS North Andean Sliver, SAM
South American Plate.

796
797
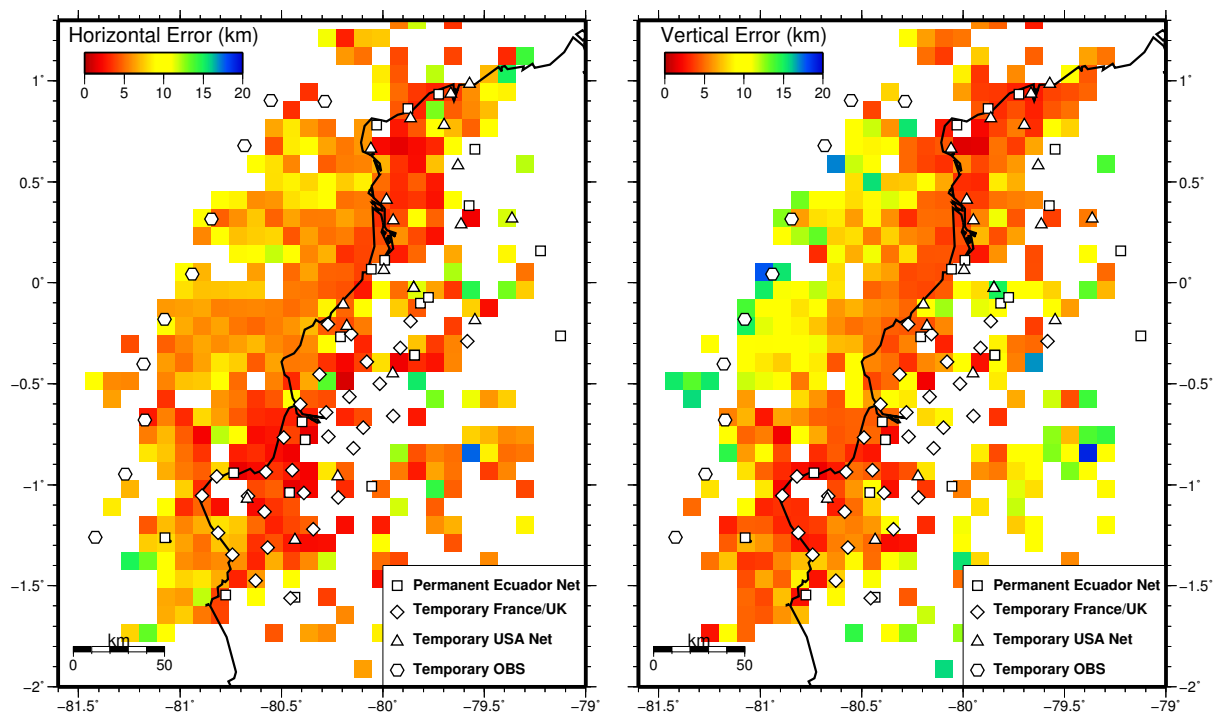
Figure 2. Seismic network and average location errors (68% confidence) for events with confidence ellipse semi-axes less than 20 km (50% of total events). Left: average horizontal error; Right: average vertical error.

798
799
800
801
802
803
804
805
806
807
808
809
810
811
812
813

815
816 **Figure 3** (previous page). Aftershock locations in map view and depth sections. Light blue
817 circles show all first quality locations; dark blue circles show high accuracy locations with
818 ellipse semi-axis errors less than 5 km. Coseismic rupture model is shown as white contours
819 every 1 m slip (Nocquet et al., 2017). Red stars are aftershocks with $M_L>=5$. Pink contours
820 show afterslip every 10 cm (Rolandone et al., 2018). Clusters (G1-G5) indicate seismicity
821 groups described in Section 3. Slab depth model (white lines in map, black line in depth
822 sections) from Hayes, 2012. Histograms with blue bars show number of earthquakes for each
823 profile. Histogram with orange line in N-S profile show distribution of coseismic slip along
824 strike.
825
826
827
828
829
830
831
832

833
834
835 **Figure 4.** GCMT mechanisms and regional moment tensors obtained in this work.
836 Distribution shows epicentral location from this study for all events, and depth from
837 computed centroid depth. Inset (top) rose histogram showing strike of nodal planes for all
838 reverse fault mechanisms. Blue segmented line shows strikes of nodal planes for mainshock.
839 Inset (bottom) shows histogram of rotational angle relative to mainshock mechanism for all
840 reverse fault events. For details, see also Table 2 in Supplementary Material.
841
842
843
844
845
846
847
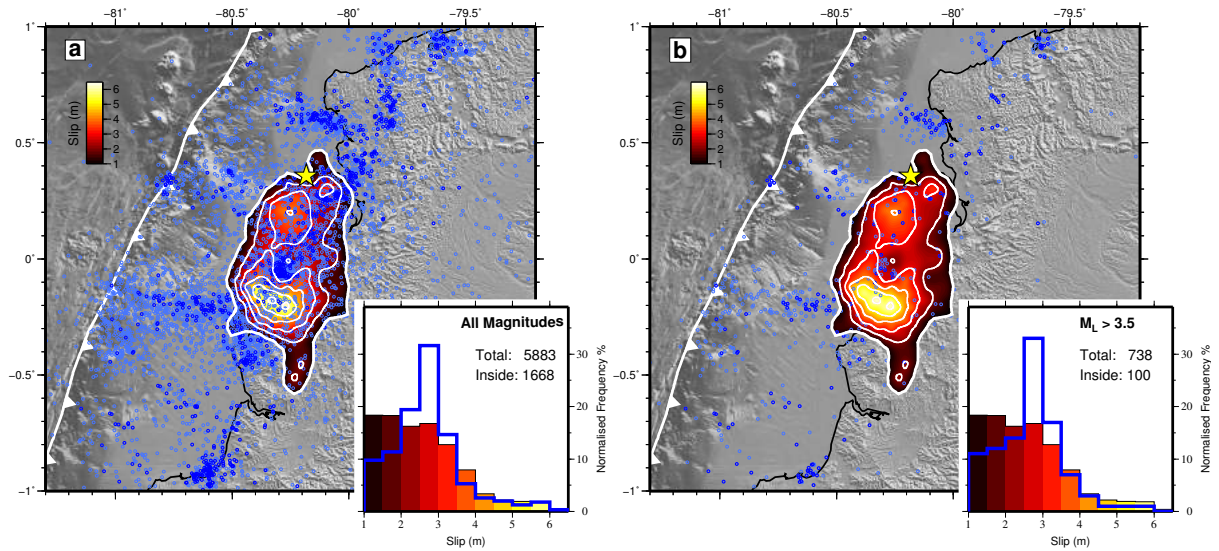
848
849
850 **Figure 5.** Distribution of aftershocks and coseismic rupture (Nocquet et al., 2017). (a) all
851 magnitudes; (b) magnitudes equal or greater than 3.5. Histograms show normalized
852 frequency distribution of coseismic slip (colour bars) and aftershocks (blue line).
853
854
855
856
857
858
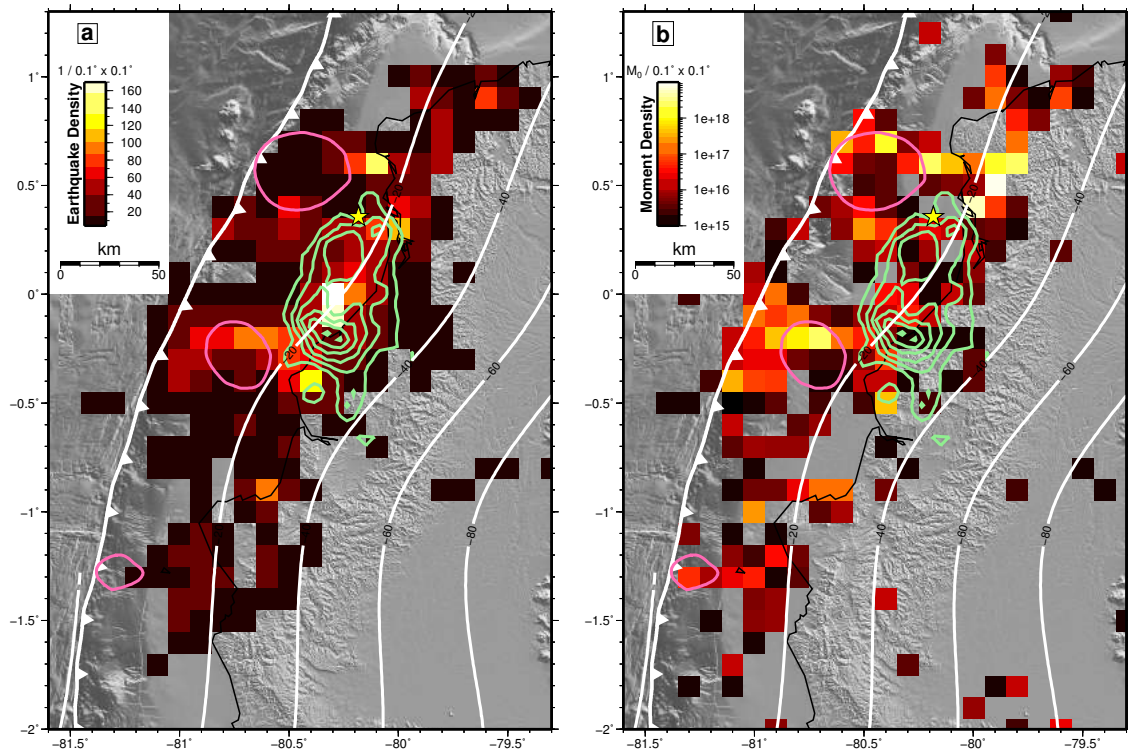
859
860
861 **Figure 6**. Density plots for (a) number of earthquakes, (b) seismic moment. Other features
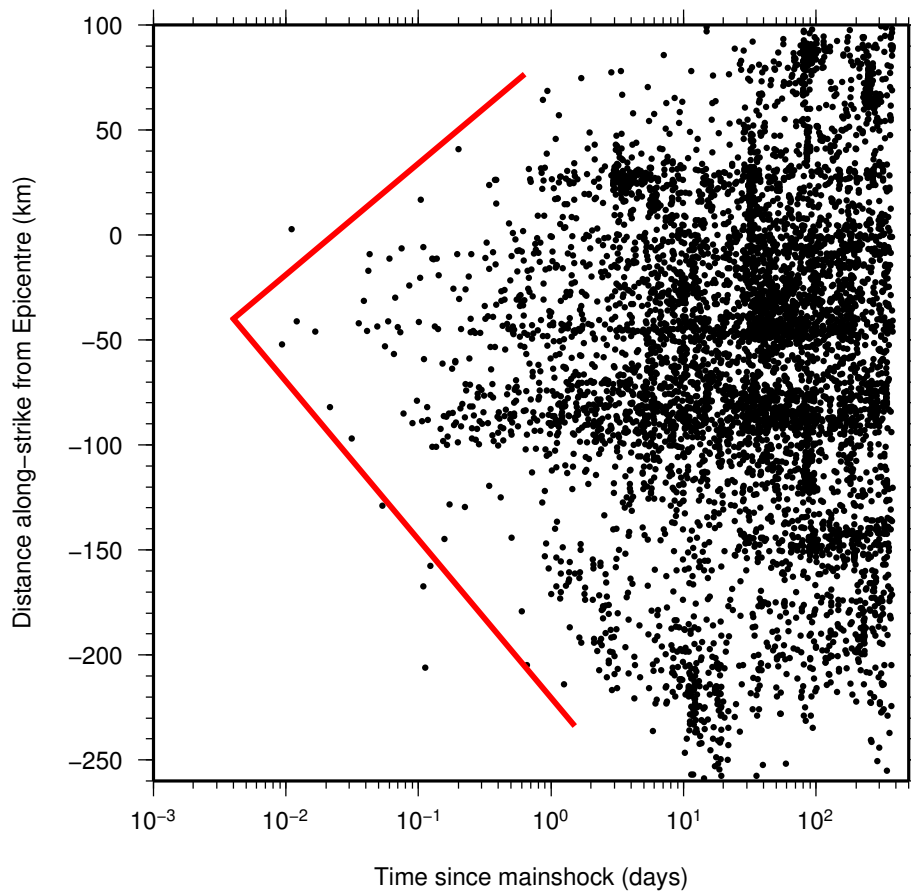862 same as in Fig. 2.
863
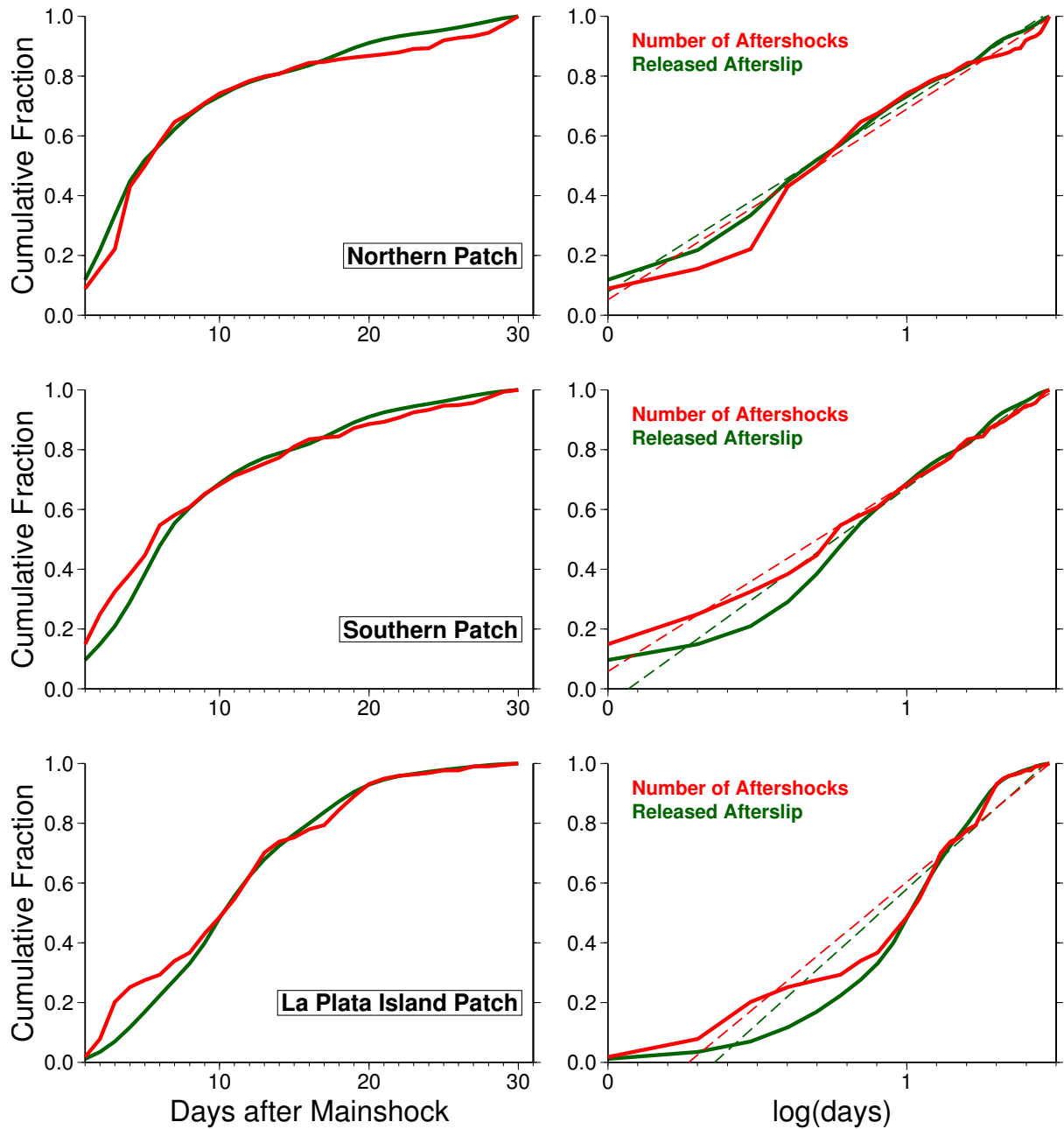
Figure 7. Temporal evolution of afterslip and aftershocks for the three different afterslip patches during the first 30 days following the mainshock. Released afterslip distribution after Rolandone et al. (2018). Left panels: cumulative distribution as a function of day. Right panels: cumulative distribution as a function of logarithm of day. Segmented line is best-fitted straight-line.
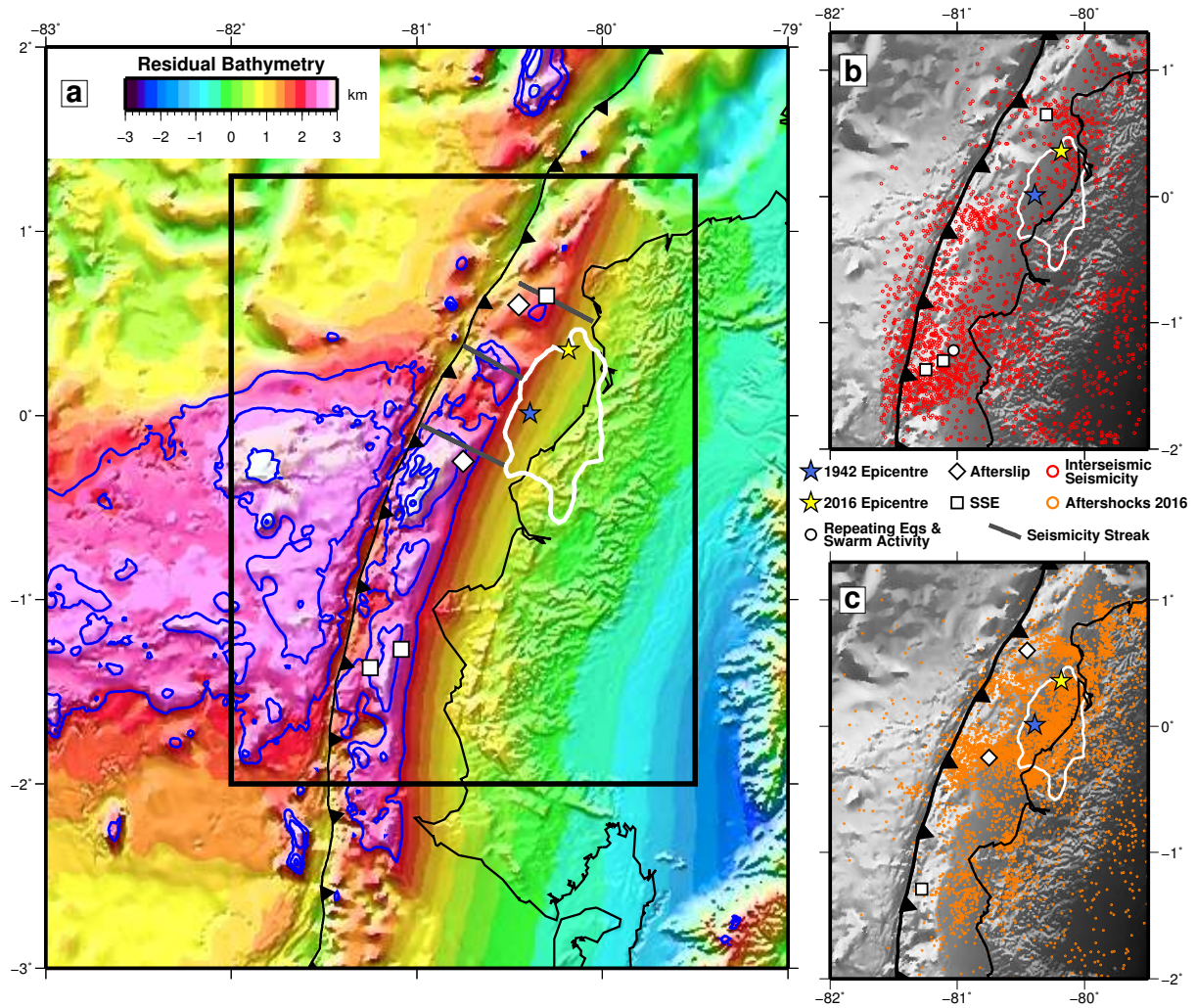
Figure 8. Expansion of earthquakes along strike in function of time since the mainshock. Red line indicates semi-logarithmic migration velocity of events (drawn by hand).
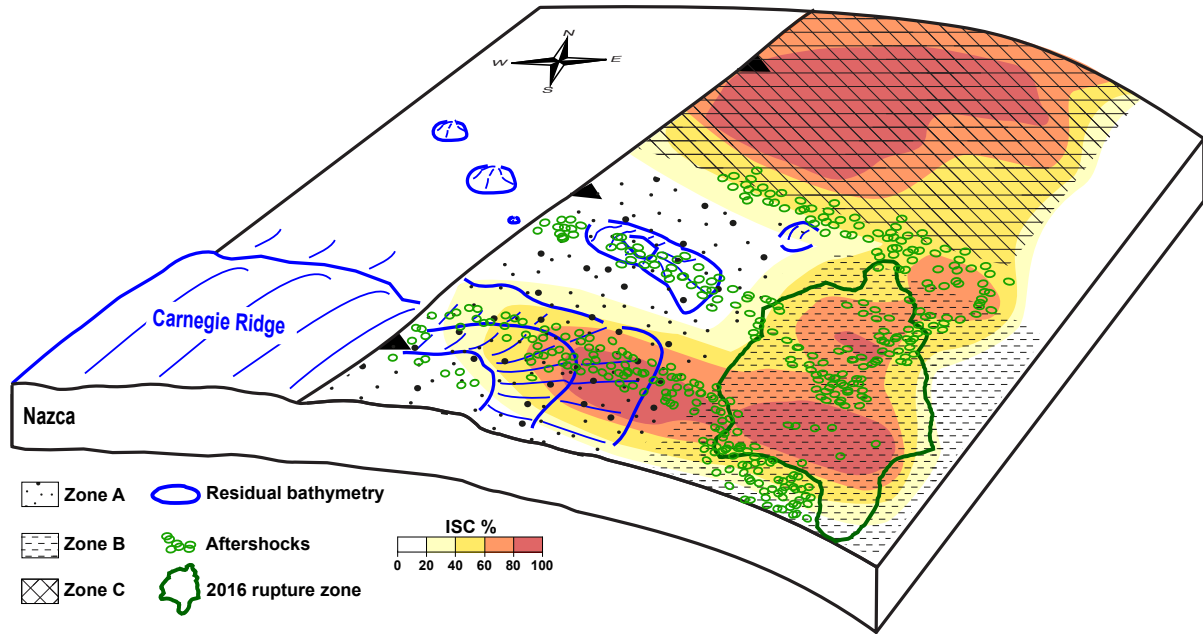
881
882
883
884
885
886
887
888
889
890
891
892
893
894
895
896
897
898
899
900
901
902
903
904
905

Figure 9. (a) Residual bathymetry and slip processes in the Ecuadorian margin. Blue contours every 500 m above 2000 m of residual bathymetry. Black box shows zoomed area in right-side panels. (b) interseismic (1943-2016) slip processes over residual bathymetry in grey scale. Seismicity from ISC catalogue. (c) postseismic slip processes (after 2016 mainshock) over residual bathymetry in grey scale.

929

930
931
932
933 **Figure 10.** Schematic summary figure. We propose that the area influenced by the
934 subduction of the CR, as shown by the residual bathymetry contours, delimits the slip mode
935 along dip and along strike in the Ecuadorian margin. Along dip, Zone A presents a rough and
936 highly heterogeneous interface with the presence of fractures, possible fluids and overall low
937 coupling. The interface at Zone A would be weak and seismically stable (velocity
938 strengthening), and its slip mode is dominated by creeping, and includes SSE, repeating
939 earthquakes, small to medium size (M<6) earthquakes and swarm activity, including the
940 permanent bands of seismicity. Down dip, Zone B is less influenced by the CR, presenting an
941 overall high coupling and a smoother interface allowing for large megathrust ruptures,
942 although contained within ~15 to 40 km depth as in the case of the 1942 and 2016 ruptures.
943 North of the CR along strike, Zone C is out of the influence of the CR and presents overall
944 high ISC and large (M>7.5) megathrust ruptures that occasionally can reach the trench as in
945 the case of the 1906 earthquake. The interfaces of both Zones B and C therefore would be
946 unstable/conditionally stable (velocity weakening).
947
948
949
950
951
952
953
954
955
956

957